HYDROGEN RELEASE FROM A HIGH-PRESSURE GH2 RESERVOIR IN CASE OF A SMALL LEAK

Xiao J. [1], Travis J.R.[2], Breitung W.[1],
[1] Research Center Karlsruhe, P.O. Box 3640, 76021 Karlsruhe, Germany
[2] DuBois, Pitzer, Travis GmbH, Offenbach, Germany

ABSTRACT

High-pressure GH_2 systems are of interest for storage and distribution of hydrogen. The dynamic blow-down process of a high-pressure GH_2 reservoir in case of a small leak is a complex process involving a chain of distinct flow regimes and gas states which needs to be understood for safety investigations.

This paper presents models to predict the hydrogen concentration and velocity field in the vicinity of a postulated small leak. An isentropic expansion model with a real gas equation of state for normal hydrogen is used to calculate the time dependent gas state in the reservoir and at the leak position. The subsequent gas expansion to 0.1 MPa is predicted with a zero-dimensional model. The gas conditions after expansion serve as input to a newly developed integral model for a round free turbulent H_2-jet into ambient air. The model chain was evaluated by jet experiments with sonic hydrogen releases from different reservoir pressures and temperatures.

Predictions are made for the blow-down of hydrogen reservoirs with 10, 30 and 100 MPa initial pressure. The evolution of the pressure in the reservoir and of the H_2 mass flux at the orifice are presented in dimensionless form, which allows scaling to other system dimensions and initial gas conditions. Computed hydrogen concentrations and masses in the jet are given for the 100 MPa case. A normalized hydrogen concentration field in the free jet is presented which allows for a given leak scenario the prediction of the axial and radial range of burnable H_2-air mixtures.

1. INTRODUCTION

In a future hydrogen economy, hydrogen will be generated from a variety of primary energy sources like e.g. solar, wind, water and nuclear fission. Hydrogen will serve as the secondary energy carrier which needs to be stored and distributed according to time and space dependent energy demands from industry, commerce, house holds, the transportation sector and others. For all gaseous storage and distribution systems a high hydrogen pressure is attractive because this increases the energy density and energy transport capacity.

The risk assessment for such high pressure GH_2 system must address the consequences of unintended leak scenarios which require an understanding of the hydrogen distribution and mixing processes with air. This paper investigates important safety parameters of unignited jets from a small leak, namely axial and radial range of burnable H_2 – air mixtures, total burnable volume, burnable mass, and range of mixtures with flame acceleration potential. These jet properties can be used to define safety distances and appropriate risk reduction measures.

2. DESCRIPTION OF NUMERICAL MODELS

The dynamic blow-down process of a high-pressure GH_2 reservoir in case of a small leak involves a sequence of distinct flow regimes and gas states as shown in Fig. 1.

Phase 1: Release of high pressure hydrogen from a reservoir through a postulated small leak;

Phase 2: Adiabatic expansion to atmospheric pressure;

Phase 3: Free turbulent H_2-jet into ambient air from the virtual jet origin.

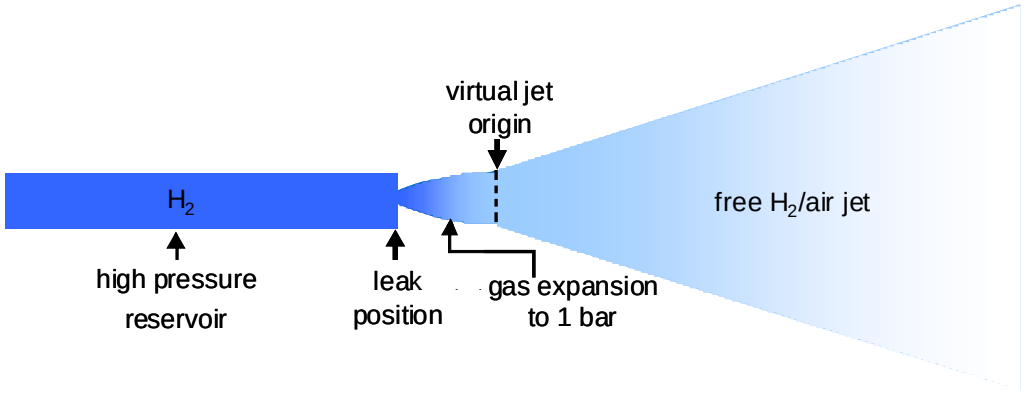

Fig. 1: Sequence of flow regimes in the dynamic blow-down process
of a high-pressure GH_2 reservoir in case of a small leak.

2.1 Discharge from a high pressure reservoir

The analysis of the hydrogen discharge from a high pressure reservoir requires a real gas equation of state for correct modeling of the thermodynamics.

2.1.1 Hydrogen Real Gas Equation of State

Modern equations of state[1,2] are often formulated using the Helmholtz energy as the fundamental property with independent variables of temperature and density,

$$\alpha(T,\rho) = \alpha^0(T,\rho) + \alpha^r(T,\rho), \tag{1}$$

where $\alpha(T, \rho)$ is the Helmholtz energy, $\alpha^0(T, \rho)$ is the ideal gas contribution to the Helmholtz energy, and $a^r(T, \rho)$ is the residual Helmholtz energy which corresponds to the influence of intermolecular forces. Thermodynamics properties can be calculated as derivatives of the Helmholtz energy. In practical applications, the functional form is explicit in the dimensionless Helmholtz energy, a, using independent variables of dimensionless density and temperature. The form of this equation is

$$\frac{\alpha(T,\rho)}{RT} = \alpha(\tau,\delta) = \alpha^0(\tau,\delta) + \alpha^r(\tau,\delta), \tag{2}$$

where $\tau = T_c/T$ is the inverse reduced temperature, T_c is the critical temperature, $\delta = \rho/\rho_c$ is the reduced density, and ρ_c is the critical density.

The ideal gas Helmholtz energy is represented in the computational convenient parameterized form

$$\alpha^0(\tau,\delta) = \ln\delta + 1.5\ln\tau + a_1 + a_2\tau + \sum_{k=3}^{N} a_k \ln\left[1 - \exp(b_k\tau)\right], \tag{3}$$

and the residual contribution to the Helmholtz free energy takes the form

$$\alpha^r(\tau,\delta) = \sum_{i=1}^{l} N_i \delta^{d_i} \tau^{t_i} + \sum_{i=l+1}^{m} N_i \delta^{d_i} \tau^{t_i} \exp\left(-\delta^{p_i}\right) + \sum_{i=m+1}^{n} N_i \delta^{d_i} \tau^{t_i} \exp\left[+\varphi_i (\delta - D_i)^2 + \beta_i (\tau - \gamma_i)^2\right], \tag{4}$$

where the parameters and coefficients for parahydrogen and normal hydrogen are given by Leachman [1,2]. The advantage of this new explicit formulation of the Helmholtz free energy is that the various properties, such as the pressure, compressibility factor (Fig. 2), enthalpy, entropy, speed of sound (Fig. 3), internal energy, Gibbs energy and isochoric heat capacity, can be calculated from partial derivatives.

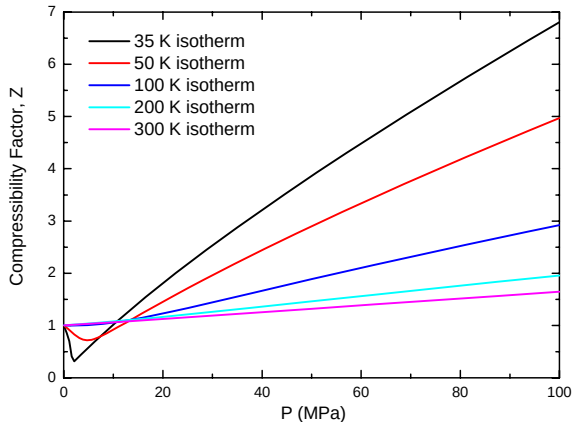

Fig. 2: Calculated compressibility factor with Leachman's NIST hydrogen equation of state.

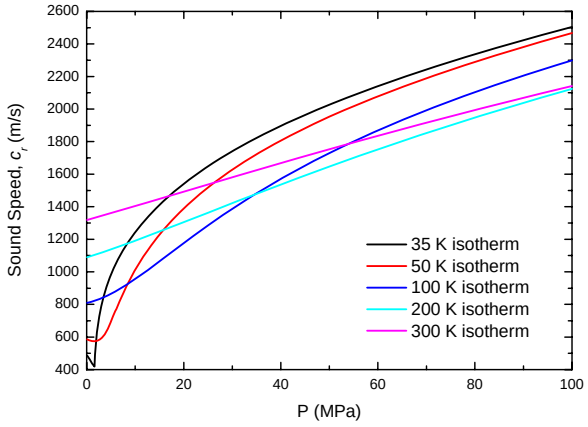

Fig. 3: Calculated sound speed with Leachman's NIST hydrogen equation of state.

2.1.2 Discharge Analysis of a High Pressure Reservoir

We can write the macroscopic mechanical energy balance for a frictionless reversible adiabatic system (an isentropic process) as the Bernoulli equation [3]

$$\int \frac{dv^2}{2} + \int \frac{dp}{\rho} = 0. \tag{5}$$

The upsteam reservoir variables, where the velocity is often assumed zero at location "*r*", at any instant are considered in a quasi-steady-state and as such, the velocity at a downstream exit location "e" can be expressed in terms of the integral along a streamline in Eq. (5) outside the boundary layer flow to yield

$$v_e = \left[-2\left(\frac{p_r}{\rho_r}\right)\int_1^{\frac{p_e}{p_r}} \left(\frac{\rho_e}{\rho_r}\right)^{-1} d\left(\frac{p_e}{p_r}\right) \right]^{\frac{1}{2}}. \tag{6}$$

At this exit location "*e*", the discharge mass flux is then

$$G_e = \rho_e v_e. \tag{7}$$

The task is to find the maximum of this function, that is, to find the pressure, P_e, so that the mass flux is maximum, which is the definition of the classical critical flow or choked condition. Should the maximum occur at the lowest pressure in the system, the flow is considered subcritical. In either case, the correct flow condition must be determined before the discharge dynamics can be computed by

$$-Vol\frac{d\rho_r}{dt} = C_D \cdot A_0 \cdot \mathbf{MAX}\left[G_e\right], \tag{8}$$

where Vol is the reservoir volume, A_0 is the break area and C_D is the discharge coefficient.

Using the equation of state from the previous section, a table of densities and pressures can be computed along an isentropic line from the stagnation conditions to the ambient pressure. With this table, Eq. 6 can be numerically integrated for each paired pressure and density in the table for successively decreasing pressures. The maximum mass fluxes from Eq. 6 are then determined for each of the paired tabular pressure and densities. With the completed table, Eq.8 is solved with any ordinary differential equation solver where the pressure, density, mass flux table is interpolated for

intermediate values. The numerical integration of Eq. 8 continues until the reservoir pressure equals the ambient value.

2.2 Adiabatic expansion

There are several investigations addressing the expansion from the actual nozzle to the virtual nozzle where the pressure becomes equal to the ambient pressure. Birch[4,5] studied underexpanded natural gas jets from a convergent nozzle and developed a model to calculate the parameters at the "pseudo-diameter". Schefer's approach[6] to study the high pressure, underexpanded hydrogen jet is entirely analogous to that of Birch in which only the conservation of mass and momentum are used to develop an expression for the notional nozzle diameter. In this approach the energy equation is not solved, and the temperature at the virtual nozzle T_v is taken as the stagnant temperature T_r. Yuceil[7] conducted an analysis similar to Birch to establish the exit parameters of the virtual nozzle. In order to determine the temperature T_v and density ρ_v at the virtual nozzle the energy equation was solved. In Yuceil's model, the discharge coefficient of the nozzle was assumed to be unity and the ideal gas equation of state was used at the actual and the virtual nozzle.

In our notional expansion model, the compressibility factor at the actual and the virtual nozzle was considered, and the energy equation was solved to obtain the temperature at the virtual nozzle. It is assumed that there is no mass flux through the boundary of the jet in the expansion process, and that the notional expansion process is adiabatic. Then a set of equations connecting the gas state at the actual exit nozzle "e" to the virtual jet origin "v" can be formulated from the basic conservation laws:

$$\begin{cases} \rho_e(\pi D_e^2/4)v_e = \rho_v(\pi D_v^2/4)v_v \\ P_e(\pi D_e^2/4) + \rho_e(\pi D_e^2/4)v_e^2 = P_v(\pi D_e^2/4) + \rho_v(\pi D_v^2/4)v_v^2 \\ C_{Pe}T_e + \dfrac{1}{2}v_e^2 = C_{Pv}T_v + \dfrac{1}{2}v_v^2 \\ \dfrac{Z_e\rho_e T_e}{P_e} = \dfrac{Z_v\rho_v T_v}{P_v} \end{cases} \tag{9}$$

where Z_e is the compressibility factor at the actual orifice. P_v, T_v, ρ_v, v_v, D_v, C_{Pv} and Z_v are the pressure, temperature, density, velocity, diameter, specific heat capacity and compressibility factor at the virtual nozzle, respectively. The Mach number at the actual nozzle exit M_e is defined as:

$$M_e = \frac{v_e}{c_e}, \tag{10}$$

where c_e is the local sound speed:

$$c_e = \sqrt{\gamma \frac{P_e}{\rho_e}}. \tag{11}$$

Solving the conservation equations (9) yields:

$$\begin{cases} v_v = v_e\left[1 + \dfrac{w-1}{\gamma M_e^2 w}\right] \\ T_v = T_e\left[\dfrac{(\gamma+w-1)}{\gamma w} - \dfrac{(\gamma-1)}{2}\left(\dfrac{w-1}{\gamma M_e w}\right)^2\right] \\ \rho_v = \dfrac{Z_e\rho_e}{Z_v}\left[\dfrac{2\gamma^2 M_e^2 w}{2\gamma M_e^2 w(\gamma+w-1) - (\gamma-1)(w-1)^2}\right] \\ D_v = D_e\sqrt{\dfrac{Z_v}{Z_e}\dfrac{2\gamma M_e^2 w(\gamma+w-1) - (\gamma-1)(w-1)^2}{2\gamma^2 M_e^2 w + 2\gamma(w-1)}} \end{cases} \tag{12}$$

where $w = P_e/P_v = P_e/P_a$ is the ratio of pressures at the actual nozzle and the virtual nozzle, and γ is the specific heat ratio of the gas. When the compressibility factors, Z_e, Z_v, are equal to one, Eq. 12 is identical to Yuceil's model. However, for the high gas pressures of interest here, real gas effects need to be taken into account (Fig. 2).

The gas expands to the ambient pressure at the virtual nozzle. It should be noted that the notional expansion does not exist in the physical sense. Experiments and numerical simulations[14] have shown that a very complicated flow structure exists in the expansion region close to the nozzle. The aim of the present study is not the resolution of this expansion region, but rather the engineering model for the far-field downstream of the exit nozzle. Eq.12 provides a consistent link between the discharge model (Section 2.1) and the integral jet model (Section 2.3) in the sense that all three sub-models only rely on mass, energy and momentum conservation. The gas state of the virtual origin derived by Eq.12 is not necessarily equal to that of Birch's "pseudo-diameter"[4,5] where the temperature restores to the stagnation temperature in the reservoir. Lower temperature and higher speed will be obtained at the jet virtual origin with Eq.12, and the location of this virtual origin is closer to the actual orifice than Birch's "pseudo-diameter". In the integral model's calculation, very rapid velocity decay and temperature recovery will be seen in the near field (seen in Section 3) which is consistent with Birch's observations. The results of this adiabatic expansion model serve as input to an integral model for a round free turbulent H_2-jet into ambient air.

2.3 Integral model for round turbulent jet

An integral model has been developed for the description of horizontal buoyant jets with arbitrary density differences between the jet and the ambient. This non-Boussinesq model can also be used for momentum dominated flows. This section outlines the model assumptions and governing equations.

The jet formed from a round orifice discharges into the unbounded stagnant uniform ambient, as shown in Fig. 4. The density of the ambient atmosphere is ρ_a. The axis of the jet is taken as a parametrical coordinate s, and the coordinate n is taken to be normal to the axis s. θ is the angle of the s-axis with the horizontal direction. The initial density, velocity, and radius in the orifice are ρ_v, u_v, r_v. The density and velocity along the s-axis are ρ_s , u_s.

The general assumptions made for the integral model are as follows:

1) The flow is fully turbulent which means there is no Reynolds number dependence.
2) The pressure across the flow is assumed to be uniform and equal to the ambient pressure outside of the flow boundary.
3) The longitudinal turbulent transport is small compared with latitudinal convective transport.
4) The radial velocity, concentration and temperature deficiency profiles are assumed to have Gaussian distribution:

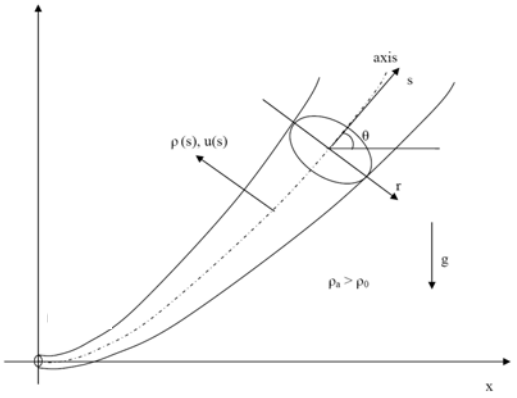

Fig. 4: Horizontal buoyant jet discharge from a round orifice into the unstratified ambient.

$$u = u_s e^{-r^2/b^2}, \tag{13}$$

where b is a characteristic radial distance from the s-axis.

The density profile with respect to the ambient density ρ_a is assumed to be of Gaussian shape:

$$\frac{\rho_a - \rho}{\rho_a} = \left(\frac{\rho_a - \rho_s}{\rho_a}\right) e^{-r^2/(\lambda b)^2}, \tag{14}$$

where λb is the characteristic length of the profiles; λ^2 is the turbulent Schmidt number. In this study λ is taken as 1.2.

The temperature profile is also assumed to have a Gaussian distribution:

$$\frac{T_a - T}{T_a} = \left(\frac{T_a - T_s}{T_a}\right) e^{-r^2/(\lambda b)^2}. \tag{15}$$

5) The entrainment relation for the round jet is given by the equation:

$$E_m = 2\pi b \rho_a u_e = 2\pi \beta_{j-p} b \rho_a u_s. \tag{16}$$

where E_m is the local mass entrainment rate, u_e is the local entrainment velocity, u_s is the characteristic velocity along the s-axis, ρ_s is the local density along the s-axis, ρ_a is the ambient density, and β_{j-p} is the local mass entrainment coefficient. The local entrainment coefficient for the round jet is assumed as [8,9]:

$$\beta_{j-p} = \left[\beta_j + (\beta_p - \beta_j)\left(\frac{Ri_{j-p}}{Ri_p}\right)^2 \sin\theta\right] * \left(\frac{\rho_s}{\rho_a}\right)^{\frac{1}{2}}, \tag{17}$$

where β_j = 0.055 for the pure jets and β_p = 0.085 for the pure plume. We should note that the value of β_j was obtained from low velocity flows. For flows with high velocity, β_j may vary. Ri_{j-p} is the local Richardson number defined as [8]:

$$Ri_{j-p} = \frac{m\phi^{1/2}}{mo^{5/4}}, \tag{18}$$

where the mass flux m is

$$m = \int_0^\infty \int_0^{2\pi} \frac{\rho}{\rho_a} urdrd\varphi = \left[\pi - \frac{\pi\lambda^2}{1+\lambda^2}\left(1 - \frac{\rho_s}{\rho_a}\right)\right] u_s b^2, \tag{19}$$

the momentum flux, mo, is

$$mo = \int_0^\infty \int_0^{2\pi} \frac{\rho}{\rho_a} u^2 rdrd\varphi = \left[\frac{\pi}{2} - \frac{\pi\lambda^2}{1+2\lambda^2}\left(1 - \frac{\rho_s}{\rho_a}\right)\right] u_s^2 b^2. \tag{20}$$

and the local buoyancy flux ϕ is

$$\phi = \int_0^\infty \int_0^{2\pi} \frac{(\rho_a - \rho)}{\rho_a} gurdrd\varphi = \frac{\pi\lambda^2}{1+\lambda^2}\left(1 - \frac{\rho_s}{\rho_a}\right) g u_s b^2, \tag{21}$$

where Ri_p is the Richardson number in the pure plume region defined as:

$$Ri_p = \sqrt{\frac{2^{4.5}\pi^{0.5}\beta_p}{5\left(1+\lambda^2\right)}}. \tag{22}$$

The basic governing equations neglecting the dissipation and turbulent transport in comparison with the mean flow consist of mass, momentum, energy and concentration conservation equations:

$$\begin{cases} \nabla\bullet(\rho\vec{u}) = 0 \\ \dfrac{\partial(\rho u u_i)}{\partial x} = 0 \\ \dfrac{\partial(\rho u u_j)}{\partial y} = \Delta\rho g \\ \nabla\bullet(\rho\vec{u}h) = 0 \\ \nabla\bullet(\rho\vec{u}\phi_m) = 0 \end{cases} \tag{23}$$

where h is the sensible enthalpy, Φ_m is the mass concentration, and $\Delta\rho$ is the density difference of the ambient and the virtual jet orifice.

When the divergence theorem is applied, the basic governing equations become:

$$\begin{cases} \dfrac{d}{ds}\int_0^{2\pi}\int_0^{\infty}(\rho u) r dr d\varphi = 2\pi\beta_{j-p} b \rho_a u_s = E_m \\ \dfrac{d}{ds}\int_0^{2\pi}\int_0^{\infty}(\rho u u\cos\theta) r dr d\varphi = 0 \\ \dfrac{d}{ds}\int_0^{2\pi}\int_0^{\infty}(\rho u u\sin\theta) r dr d\varphi = \int_0^{2\pi}\int_0^{\infty}(\rho_a - \rho) g r dr d\varphi \\ \dfrac{d}{ds}\int_0^{2\pi}\int_0^{\infty}\left[\rho u\left(C_P T - C_{Pa} T_a\right)\right] r dr d\varphi = 0 \\ \dfrac{d}{ds}\int_0^{2\pi}\int_0^{\infty}(\rho u\phi_m) r dr d\varphi = 0 \\ \dfrac{dx}{ds} = \cos\theta \\ \dfrac{dy}{ds} = \sin\theta \end{cases} \tag{24}$$

A system of first order ordinary differential equations is thus obtained after the integration of Eq. 24, where the seven unknowns are the density ρ_s, velocity u_s, temperature T_s along the trajectory, the characteristic jet width b, the local angle of the jet with respect to the horizontal axis θ, and the local coordinates of the jet trajectory x, y. With initial conditions, the system of ordinary differential equations was solved with a 4th order Runga-Kutta method to obtain the buoyant jet trajectory, the velocity, the density, the temperature and the concentration.

3. MODEL VALIDATIONS

The chain of models includes the isentropic discharge model, the adiabatic expansion model to 0.1 MPa and the non-Boussinesq integral model. Results of these models were compared to jet experiments carried out in a special FZK facility. Hydrogen was released with the steady mass flux of 3.3 g/s from orifices with diameters of 1 mm and 2 mm. Four experiments with various initial pressures and temperatures were analyzed (Table 1). The gas state in the reservoir is given in columns 2 to 4. The pressure P_r is the theoretical pressure which is calculated by the model in Section 2.1 to obtain a mass flow rate of 3.3 g/s. The results of the discharge and the adiabatic expansion model are shown in Table 1 for the actual orifice and the virtual jet origin. The parameters at the virtual jet origin served as input for the integral model. The experiments were performed under steady state conditions with sonic flow velocity at the nozzle.

Fig. 5 compares measured and calculated hydrogen concentration decays for the four test cases, using the orifice diameter D_0 as scaling parameter for the distance S from the orifice. All experimental data

and the calculated results of the integral model collapse when the scaling of the distance includes the ratio of the density in the reservoir ρ_r and the ambient atmosphere ρ_a, according to

$$D_{eq} = D_0\sqrt{\rho_r / \rho_a}\,, \tag{25}$$

where D_{eq} is the scaled orifice diameter (Fig. 6). Note that this scaling also covers the significant temperature variation in the initial jet conditions (80 K and 298 K).

Fig. 7 compares measured and predicted velocity along the jet trajectory, U_s. The velocity decelerates rapidly in the near field due to the air entrainment into the jet. At the distance S/D_0 = 300, the velocity has decreased to about 1% of the initial velocity and the volume fraction of hydrogen in the jet center is about 12.5%. This indicates that the jet is well mixed and buoyancy has little effect on the flow in the low velocity region. Fig. 8 compares PIV measured radial velocity profiles with predictions of the integral model for case 1 in Table 1. The profiles correspond to axial distances S/D_0 = 580, 300, 150, 100, 75, 50 and 25 (top to bottom in the legend). The very good agreement supports the assumption of Gaussian distributions in the integral model. Fig. 9 and Fig.10 demonstrate the rapid density and temperature recovery to the ambient conditions due to the air entrainment for the four cases specified in Table. 1.

It should be noted that in these cases the entrainment coefficient β_j was slightly increased from 0.055 to 0.070 in the integral model to achieve the best agreement with the experimental data. The value of β_j = 0.055 was obtained from experiments with low velocities and small density ratios[8,9]. It seems reasonable that higher velocity and turbulent intensity will induce a stronger mass entrainment. The non-Boussinesq integral model was also compared to literature data for slow pure jets (air into air) and for slow weakly buoyant jets (N_2 into air). Excellent agreement was found with β_j = 0.070, which confirms the predictive capabilities of the developed non-Boussinesq integral model.

Table 1. Reservoir conditions of the under-expanded hydrogen jet experiments and computed gas states for the actual orifice and the virtual jet origin after expansion to 0.1 MPa.

Cases	Reservoir			Actual orifice					Virtual jet origin			
	P_r (MPa)	T_r (K)	ρ_r (kg/m^3)	D_0 (mm)	P_e (MPa)	T_e (K)	ρ_e (kg/m^3)	v_e (m/s)	D_v (mm)	ρ_v (kg/m^3)	T_v (K)	v_v (m/s)
1	1.7	298	1.369	2	0.89	246.8	0.869	1208.9	3.76	0.151	163.3	1969.2
2	6.85	298	5.354	1	3.552	246.1	3.42	1231.4	3.52	0.163	152.8	2080.4
3	0.825	80	2.527	2	0.4	60.1	1.641	640.4	2.75	0.566	43.6	979.8
4	3.2	80	10.019	1	1.513	59.5	6.603	637.8	2.44	0.669	38.1	1060.2

4. BLOW-DOWN OF A HIGH-PRESSURE H_2 GAS RESERVOIR

In this section the above described models for the flow conditions at the break location, the notional jet expansion to 0.1 MPa and the round free jet into ambient atmosphere are applied to the simulation of a small leak in a high-pressure GH2 system.

The selected system dimensions are a pipe length of 1000 m, a pipe diameter of 10 cm and a leak diameter of 1 cm. The total system volume is 7.8 m^3. The initial temperature is 300 K and three different initial pressures are analyzed: 10, 30 and 100 MPa. Fig. 11 shows the assumed isentropic expansion path for these cases, based on the above described real-gas equation of state. Two-phase conditions are not encountered. The methodology described in Section 2.1 leads to the mass fluxes shown in Fig. 12. The dimensionless time t^+, mass flux G^+, and pressure P^+ are defined as

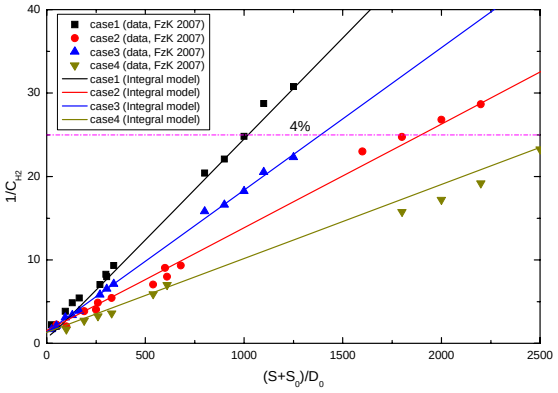

Fig. 5: Measured and calculated H_2 concentration decay along the jet axis.

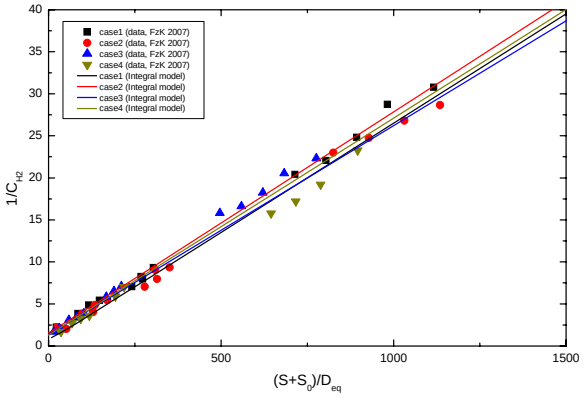

Fig. 6: H_2 concentration decay along the jet trajectory (scaled by D_{eq}).

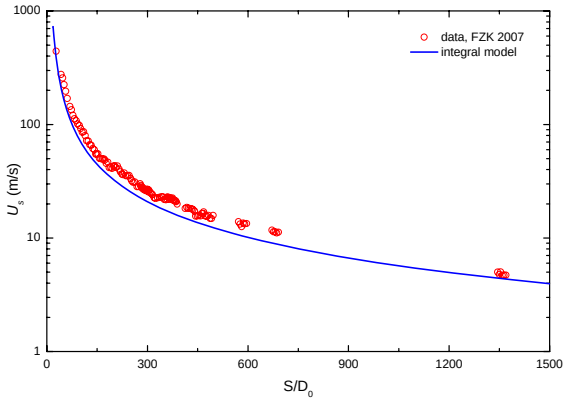

Fig. 7: Velocity decay along the jet trajectory (case 1 in Table 1).

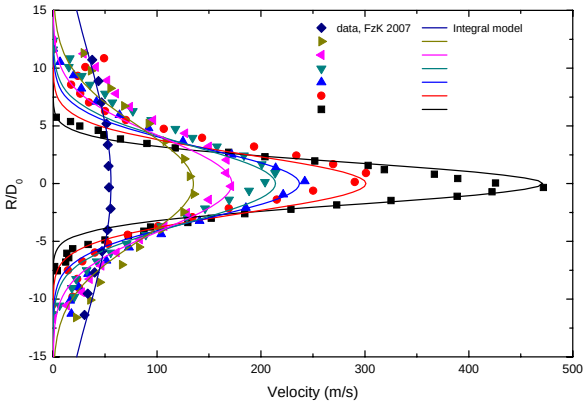

Fig. 8: Comparison of measured and calculated radial velocity profiles (case 1 in Table 1).

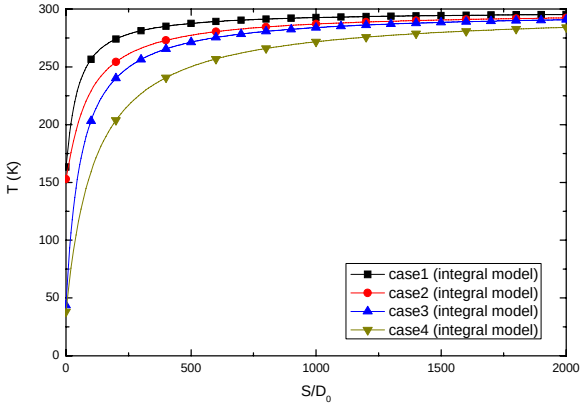

Fig. 9: Temperature recovery along the jet trajectory.

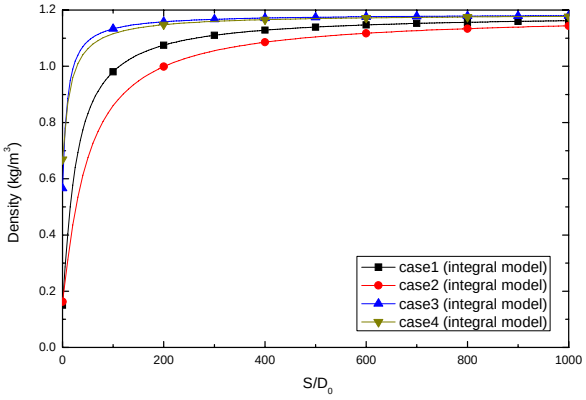

Fig. 10: Density recovery along the jet trajectory.

$$t^+ = \frac{t}{t_{char}}, \tag{26}$$

$$G^+ = \frac{G}{G_{char}}, \tag{27}$$

and

$$P^+ = \frac{P}{P_r}, \tag{28}$$

where the characteristic quantities are:

$$t_{char} = \frac{Vol}{A_0 \times c_r} \tag{29}$$

and

$$G_{char} = \rho_r \times c_r . \tag{30}$$

Here Vol is the reservoir volume, A_0 is the break area and c_r is the initial sound speed in the reservoir.

This scaling provides a close agreement of the three analyzed initial pressures. Fig. 12 allows scaling of the computed discharge mass fluxes to high-pressure systems with other volumes, break areas, initial pressures and initial temperatures for t^+ up to about 5. Fig. 13 demonstrates that the used scaling is not appropriate for $t^+ > 5$. The stars in Fig. 13 represent the times where the pressure ratio falls below 1.9 and the flow becomes sub-critical. Fig. 14 shows the dimensionless pressure decay in the tank during the discharge. Using Eq. 26 this plot allows the estimation of the pressure decay in other high pressure GH_2 systems. Note that the value $t^+ = 5$ mentioned above, corresponds to a very low remaining pressure. Table 2 summarizes the initial conditions and resulting discharge times for the present reservoir problem. Table 3 presents detailed results for the 100 MPa case. The gas conditions in the reservoir and at the leak position are given for five time points (10 s, 50 s, 100 s, 200 s, 400 s) after begin of the discharge.

Table 2: Initial conditions and resulting calculated discharge times for the three different initial pressures in the GH_2 reservoir.

Initial pressure (MPa)	Initial density (kg/m^3)	Initial sound speed (m/s)	Discharge time (s)
10	7.625	1404	593
30	20.426	1581	775
100	49.234	2142	985

Table 3: Computed gas states for the 100 MPa hydrogen blowdown for five different times after begin of the discharge.

Time (s)	Reservoir			Actual orifice					Virtual jet origin			
	P_r (MPa)	T_r (K)	ρ_r (kg/m3)	D_e (mm)	P_e (MPa	T_e (K)	ρ_e (kg/m3)	v_e (m/s)	D_v (mm)	T_v (K)	ρ_v (kg/m3)	v_v (m/s)
10	78.84	280.8	44.23	10	36.15	224.6	30.24	1511.3	99.3	136.6	0.180	2580.9
50	37.06	226.3	30.63	10	17.59	180.7	20.54	1233.4	73.5	110.1	0.223	2103.7
100	18.36	183.2	21.03	10	8.87	145.0	13.90	1043.5	54.3	88.8	0.277	1775.6
200	6.35	129.5	11.44	10	3.09	100.0	7.49	832.9	33.6	62.3	0.394	1404.7
400	1.31	72.0	4.54	10	0.64	54.1	2.99	598.7	16.8	36.9	0.666	956.4

The third part of Table 3 shows the results of the notional adiabatic expansion model described in Section 2.2. These gas states serve as input to the integral free jet model described in Section 2.3.

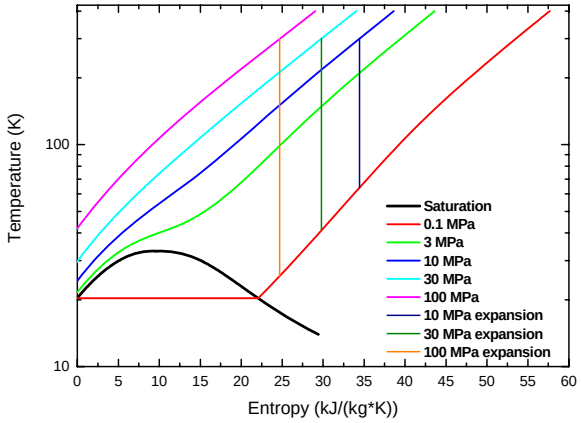

Fig. 11: Isentropic expansion processes for high-pressure hydrogen discharge cases.

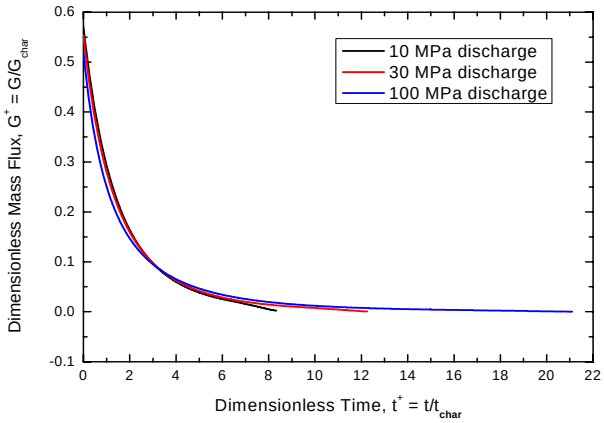

Fig. 12: Calculated dimensionless hydrogen mass flux for the three investigated discharge cases.

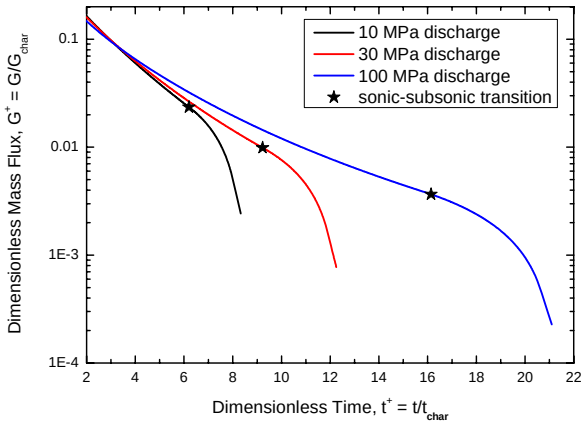

Fig. 13: Calculated dimensionless hydrogen mass flux and the sonic-subsonic transition.

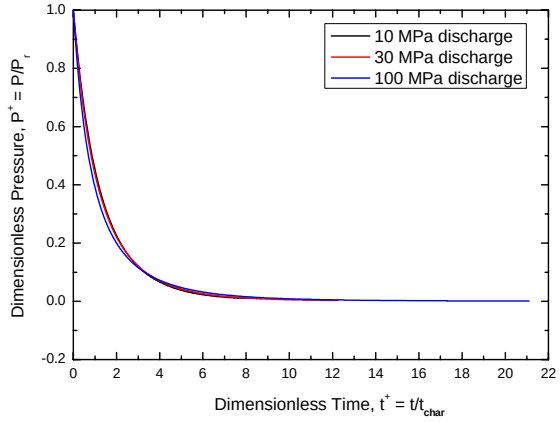

Fig. 14: Calculated dimensionless pressure in the tank for the three investigated discharge cases.

The integral model for a round free jet predicts the velocity, temperature and hydrogen concentration field downstream from the virtual jet origin. For safety investigations the hydrogen distribution in the jet is of main interest. Fig. 15 displays the computed hydrogen contours (4 to 75 vol % H_2 in air). A horizontal release direction was assumed in the calculation.

The maximum axial distance of burnable H_2-air mixtures (> 4 vol % H_2) falls from about 64 m at 10 s to about 17 m at 400 s and the corresponding maximum jet radius decreases from 7.2 to 2 m. All concentration contours in Fig. 15 are self-similar with a ratio of maximum radial to maximum axial distance of 0.111. The burnable volumes of H_2-air mixture at the five times are 651 m^3, 359 m^3, 200 m^3, 80 m^3 and 22 m^3, respectively. The corresponding hydrogen masses in the burnable part of the jet are 3.3, 1.8, 1.0, 0.4, and 0.1 kg. The horizontally oriented jet is purely momentum dominated which means there is no visible effect of buoyancy on the horizontal jet trajectory. The depicted hydrogen concentration field is therefore independent of the release direction.

Fig. 15 demonstrates that in round unignited jets from high pressure systems with sonic outflow into a free environment, the air entrainment is sufficient to dilute the released hydrogen down to unburnable mixtures within the jet flow field. No plume with burnable mixtures will remain further downstream; an additional combustion risk in the far field is excluded. The space region with hydrogen concentrations above 10 vol % is of special interest because ignition in this region leads to a stable

turbulent diffusion flame which propagates back towards to the hydrogen leak. Ignitions at lower concentrations only lead to a transient local burn which is convected downstream and quenches in regions with less than 4 vol% H_2[15].

It is well known that for the momentum dominated subsonic incompressible turbulent free jets the concentration decay along the jet centerline complies with a hyperbolic law[11]:

$$C_s = \frac{KD_0}{S + S_0}\left(\frac{\rho_a}{\rho_r}\right)^{0.5}, \tag{31}$$

where C_s is the centerline concentration, K is the slope which gives the decay constant, and S_0 is the virtual origin displacement.

Birch's study[4,5] has shown that this concentration decay law can be applied to underexpanded jets with choked-flow releases. In Houf and Schefer's work[12], Eq. 31 was also used to calculate the concentration decay of high pressure supercritical choked-flow releases of hydrogen.

The integral jet model described in Section 2.3 and the FZK experimental data give the following relation for the normalized centerline concentration decay of the hydrogen jet, as shown in Fig. 6:

$$C_{s,\mathrm{H_2}} \approx 37.6\frac{D_{eq}}{S + S_0}. \tag{32}$$

The normalized diameter D_{eq} is defined as:

$$D_{eq} = D_0\left(\frac{\rho_r}{\rho_a}\right)^{0.5}. \tag{33}$$

The virtual origin displacement S_0 will be further discussed in Section 5. If we take $S_0 = 30D_0$, the following non-dimensional axial distances, S, from the nozzle are obtained for

- the lower flammability limit:

$$S\left(4\%\mathrm{H_2}\right) = 975D_{eq}, \tag{34}$$

- the region of stable ignition:

$$S\left(10\%\mathrm{H_2}\right) = 378D_{eq}, \tag{35}$$

- the upper flammability limit:

$$S\left(75\%\mathrm{H_2}\right) = 34D_{eq}. \tag{36}$$

The axial distances in Fig. 15 for the 4%, 10% and 75% H_2 contours agree well with these correlations. Eqs. (33-36) can be applied to other free round high-pressure jets to estimate the axial range of burnable mixtures. The corresponding maximum radial extensions of burnable mixtures, R_{rad}, are approximately

$$R_{rad} \approx 0.111S \tag{37}$$

For any given time in Fig. 15 the axial distances S are proportional to $(\rho_r/\rho_a)^{0.5}$ and the burnable volumes are proportional to $(\rho_r/\rho_a)^{1.5}$ due to the self-similar structure of the jet. Fig. 16 shows the normalized hydrogen concentration contours. When scaled by D_{eq}, all the contours in Fig. 15 collapse closely to the contours in Fig. 16, which is useful to estimate the maximum burnable radius and length of an underexpanded hydrogen jet.

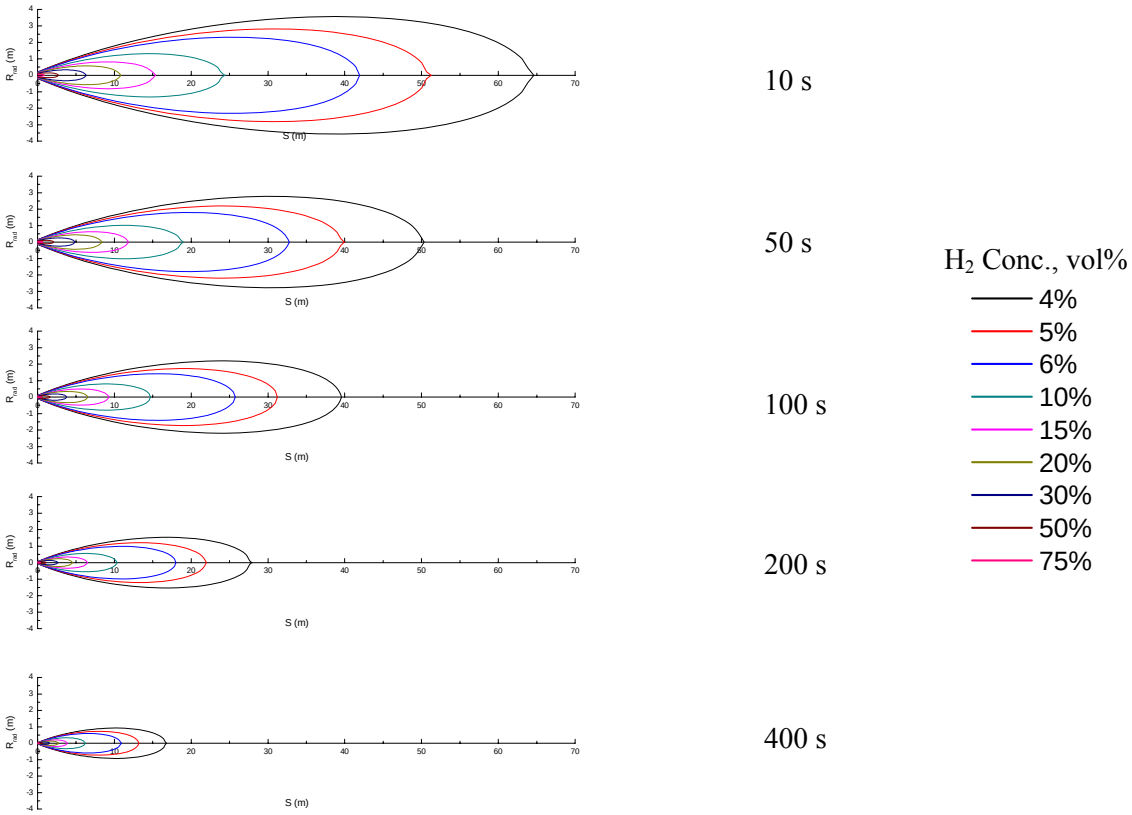

Fig. 15: Computed hydrogen concentration field of free round jets from a 100 MPa hydrogen reservoir for different times after discharge (reservoir conditions in Table 3).

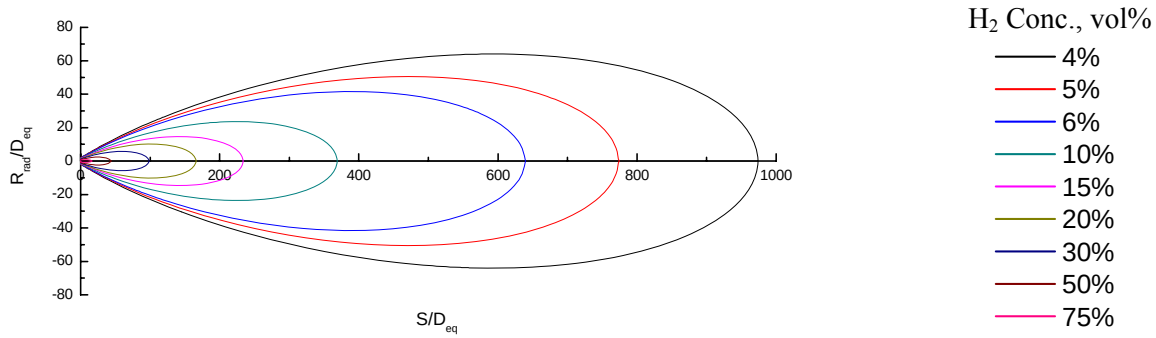

Fig. 16: Normalized hydrogen concentration contours of a free hydrogen jet with sonic discharge (scaled by D_{eq}).

5. MODELING UNCERTAINTIES

Most of the published integral models based on Gaussian distributions and the Boussinesq approximation were validated by experiments with low jet exit velocities and small density variations. In our integral model the Boussinesq approximation was not used, so that the model is valid for cases with large density variations [13]. This model can be used for buoyant jets which are influenced by both the momentum and the buoyancy, as well as underexpanded jets which are dominated by the momentum. However, the mass entrainment coefficient β_j used in the integral model was obtained under the experimental conditions with low velocity and density variation. In the simulation of the under-expanded hydrogen jet experiment in Section 3.4, it was found that the entrainment coefficient β_j for the pure jet increases from 0.055 to 0.07 to obtain the best agreement with the experimental data. Although it seems reasonable that higher velocity and turbulent intensity will introduce a stronger

mass entrainment, the effect of the high velocity and large density variation on the entrainment coefficient needs further study.

Before the Gaussian profiles are established, the initial unsheared profiles undergo changes in form of peripherally growing axis symmetric mixing layers. This initial region is called the zone of flow establishment (ZOFE) which lacks self-similarity. The transition in this region is complex and rapid. For the low speed flow the distance extends up to 5~10 D_0 from the orifice [9]. In Xu's numerical simulation of under-expanded hydrogen jet[14] $30D_0$ from the real orifice is found to be a critical location which marks the end of the shock structure and the near field expansion of the jet, and the location of the Mach disk is roughly at $10D_0$ with a diameter at 5.6 D_0. In our study, the integral model's virtual origin displacement S_0 is $5D_0$ for the subsonic flow. For sonic or supersonic flow S_0 is about $15\sim30D_0$ depending on the pressure ratio between the reservoir and the ambient. Further study of the virtual origin displacement for underexpanded jets is desirable. However the far field predictions made in this study will not be affected significantly because the burnable hydrogen jet extends to a long distance away from the orifice.

A further issue in the non-Boussinesq integral model is to verify the hydrogen volume fraction at the location where the self-similar flow is established, which serves as input to the model. In the Boussinesq-based integral model, since the density difference between the jet and the ambient can be neglected the volume fraction at this location can be assumed as 100%. However, large density variation between the jet and the ambient might lead to a mass fraction below 100% due to the mass entrainment in this transition region. Xu's numerical simulation[14] for an under-expanded hydrogen jet into air indicates that there is no air entrainment prior to the Mach disk, and at the location $30D_0$ the H_2 volume fraction is nearly unity. In the present integral model analysis, the initial volume fraction of hydrogen at the virtual origin is assumed unity.

Another uncertainty is the discharge coefficient which is case sensitive. It depends on the system pressure, temperature and break parameters like shape, size, and wall thickness. It represents an important uncertainty for any accident simulation and some separate estimation of discharge coefficient should be attempted. We compared the measured and the theoretical mass flow rates in our cases, and there is only 10% deviation between the measured and theoretical. In the study, we assume that the discharge coefficient is 1.0 which is conservative for the safety analysis.

6. CONCLUDING REMARKS

A chain of engineering models for hydrogen jet from a small leak of a high pressure pipeline has been developed and verified by the FZK measured concentration and velocity decay along the centerline of underexpanded hydrogen jet. The newest real gas equation of state was applied to calculate the discharge of high pressure hydrogen through a postulated small leak. An adiabatic expansion model considering the energy equation and the compressibility factor was used to obtain the parameters at the virtual origin as the input for the integral model. A non-Boussinesq integral model with an entrainment coefficient adjusted to sonic H_2-jet experiments was developed to calculate the concentration, velocity and temperature variation along the centerline, the burnable length, width and volume for the safety analysis. The derived non-dimensional results can be scaled to other high-pressure systems using the given relations.

ACKNOWLEDGEMENT

Part of this work was performed within the ICEFUEL project (www.icefuel.eu) which is funded by the German BMBF ministry. The authors are indebted to Jacob Leachman for his extraordinary help and support with the real gas equation of state.

REFERENCES

1. J. Leachman, Fundamental Equations of State for Parahydrogen, Normal Hydrogen, and Orthohydrogen, Master of Science Thesis, University of Idaho

2. J.W. Leachman, R.T. Jacobson, E.W. Lemmon, Fundamental Equations of State of Parahydrogen, Normal Hydrogen, and Orthohydrogen, to be published in J. Phys. Chem. Ref. Data, 2009.
3. R.B. Bird, W.E. Stewart, E.N. Lightfoot, Transport Phenomena 2nd Ed., pp 472, 2002.
4. A.D. Birch, D.R. Brown, M.G. Dodson, F. Swaffield, The Structure and Concentration Decay of High Pressure Jets of Natural Gas, Combustion Science and Technology Vol. 36, pp. 249-261, 1984.
5. A.D. Birch, D.J. Hughes, F. Waffield, Velocity Decay of High Pressure Jets, Combustion Science and Technology, Vol. 52, pp. 161-171, 1986
6. Schefer, R. W., Houf, W. G., Williams, T. C., Bourne, B., & Colton, J. (2007). Characterization of high-pressure, under-expanded hydrogen-jet flames. International Journal of Hydrogen Energy, 32(12), 2081–2093
7. K. Bülent Yüceil, M. Volkan Ötügen, Scaling Parameters for Underexpanded Supersonic Jets, Physics of Fluids, Vol. 4, No. 12, pp. 4206-4215, December 2002
8. W. Rodi, Turbulent buoyant jets and plumes, vol. 6,HMT The Science & Applications of Heat and Mass Transfer, Pergamon Press, 1982
9. G.H. Jirka, Integral Model for Turbulent Buoyant Jets in Unbounded Stratified Flows. Part I Single Round Jet, Environmental Fluid Mechanics 4: 1-56, 2004
10. G.H. Jirka, Integral Model for Turbulent Buoyant Jets in Unbounded Stratified Flows Part 2 Plane Jet Dynamics Resulting from Multiport Diffuser Jets, Environmental Fluid Mechanics 6: 43-100, 2006
11. C. Chen, W. Rodi, Vertical Turbulent Buoyant Jets – A Review of Experimental Data, Pergamon Press, 1980
12. W.G. Houf and R.W. Schefer, Predicting Radiative Heat Fluxes and Flammability Envelopes from Unintended Releases of Hydrogen, International Journal of Hydrogen Energy, Vol. 32, pp. 136-151, January 2007.
13. J. Xiao, J. Travis, W. Breitung, Non-Boussinesq Integral Model for Horizontal Turbulent Strongly Buoyant Plane Jets, Proceedings of the 16th International Conference on Nuclear Engineering, Orlando, Florida, USA, May 11-15, 2008
14. B. Xu, J. Zhang, J. Wen, S. Dembele, J. Karwatzki, Numerical study of a highly under-expanded hydrogen jet, International Conference on hydrogen Safety, Sep. 8-10, 2005, Pisa, Italy
15. A. Veser, G. Stern, M. Schwall, N. Kotchourko, M. Rottenecker, G. Fast, M. Kuznetsov, W. Breitung, Structure and Flame Propagation Regimes in Turbulent Hydrogen Jets. Proceedings of 7th International Symposium on Hazards, Prevention, and Mitigation of Industrial Explosions, Saint-Petersburg, Russia, July 7-11, 2008, Vol. 1, pp. 198-207